

Frequency Domain Tomography in Small Animals with the Equation of Radiative Transfer

Kui Ren^a, Bryte Moa-Anderson^b, Guillaume Bal^a, Xuejun Gu^b, Andreas H. Hielscher^{b,c}

^aDept. of Appl. Physics & Appl. Mathematics, Columbia University, New York, NY 10027

^bDepartment of Biomedical Engineering, Columbia University, New York, NY 10027

^cDepartment of Radiology, Columbia University, New York, NY 10027

ABSTRACT

We have developed a model-based iterative image reconstruction scheme based on the equation of radiative transfer in the frequency domain for the applications in small animal optical tomographic imaging. To test the utility of such a code in small animal imaging we have furthermore developed a numerical phantom of a mouse. In simulation studies using this and other phantoms, we found that to make truly use of phase information in the reconstruction process modulation frequencies well above 100 MHz are necessary. Only at these higher frequencies the phase shifts introduced by the lesions of interest are large enough to be measured. For smaller frequencies no substantial improvements over steady-state systems are achieved in small geometries typical for small animal imaging.

Keywords: Optical tomography, equation of radiative transfer, small animal imaging, discrete ordinate, finite volume method, inverse problems

1. INTRODUCTION

In recent years the interest in small animal imaging has increased substantially.¹⁻⁶ There exist now a great number of animal models for various diseases, such as cancer, arthritis, and stroke, that can be used to study drug efficacies and fundamental diseases development and progression. Besides systems based on more traditional medical imaging modalities such as micro PET, micro CT, MRI, and SPECT, optical tomographic small animal imaging is currently pursued by several groups.⁷ Optical tomography offers unique opportunities to measure and monitor parameters such as oxy- and deoxy-hemoglobin as well as blood volume and saturation.⁸⁻¹¹ In addition, optical molecular imaging that makes use of the many optical fluorescent and bioluminescent markers is of great interest.^{12,13}

A major challenge toward small animal optical tomography is the development of appropriate image reconstruction schemes. Because of the small tissue volumes, the diffusion equation is of limited use, thus more accurate models of light propagation are necessary. Furthermore, it is generally believed that frequency-domain methods allow for a better separation between the scattering and absorption properties of the inclusions.¹⁴ These two facts motivate us to develop a model-based iterative image reconstruction scheme that employs the equation of radiative transfer (ERT) in the frequency domain.

In this paper we first introduce the frequency domain equation of radiative transfer and present the numerical methods we employed to discretize the ERT. This is followed by a description of how the reconstruction problem is solved. We also provide details concerning a numerical mouse model that was developed to simulated light propagation in small animals. In the results section we present examples of forward calculation as well as image reconstruction using the mouse model. A summary of the main results concludes this paper.

The authors can be reached by the following E-mails.

KR: kr2002@columbia.edu and AHH: ahh2004@columbia.edu.

2. METHODS

2.1. The forward model

The propagation of near infrared light in tissues is in general best modeled by the equation of radiative transfer (ERT). Although the diffusion equation, which is the first order approximation of the ERT in the limit of optically thick media with $\mu_a \ll 1$ and $\mu_s \gg 1$, is much easier to solve and computationally less expensive, it is of limited use in small animal imaging. Several studies have described the limitations of diffusion-based algorithms in cases of media that are optically thin, that have an absorption coefficient comparable in value to the scattering coefficient, or that contain void-like inclusions.¹⁵⁻²⁰ All three situations are often encountered in small animal imaging.

The frequency-domain equation of radiative transfer that describes the photon density in the phase space, i.e., as a function of position $\mathbf{x} \in \mathcal{D} \subset \mathbb{R}^n$ and direction $\boldsymbol{\theta} \in S^{n-1}$ (unit sphere of \mathbb{R}^n) is given by²¹

$$\begin{aligned} \left(\frac{i\omega}{v} + \boldsymbol{\theta} \cdot \nabla + \mu_a(\mathbf{x}) \right) u(\mathbf{x}, \boldsymbol{\theta}) + Q(u)(\mathbf{x}, \boldsymbol{\theta}) &= 0 && \text{in } \mathcal{D} \times S^{n-1} \\ u(\mathbf{x}, \boldsymbol{\theta}) &= f(\mathbf{x}, \boldsymbol{\theta}) && \text{on } \Gamma_-, \end{aligned} \quad (1)$$

where $i = \sqrt{-1}$, $n = 2, 3$ is the space dimension, $v \in \mathbb{R}^+$ is the speed of light in the medium, and ω is the modulation frequency of the boundary source $f(\mathbf{x}, \boldsymbol{\theta})$. The non-negative function $\mu_a(\mathbf{x}) \in L^\infty(\mathcal{D})$ is the absorption coefficient. The unknown quantity, $u(\mathbf{x}, \boldsymbol{\theta})$, is the radiant power per unit solid angle per unit area perpendicular to the direction of propagation at \mathbf{x} in the direction $\boldsymbol{\theta}$. Note that we have dropped the explicit dependence of $u(\mathbf{x}, \boldsymbol{\theta})$ on ω to simplify the notation. The boundary sets Γ_- are defined as

$$\Gamma_- = \{(\mathbf{x}, \boldsymbol{\theta}) \in \partial\mathcal{D} \times S^{n-1} \text{ s.t. } \boldsymbol{\theta} \cdot \boldsymbol{\nu}(\mathbf{x}) < 0\},$$

with $\boldsymbol{\nu}(\mathbf{x})$ the outward unit normal to the domain at $\mathbf{x} \in \partial\mathcal{D}$. The scattering operator Q is defined as

$$Q(u)(\mathbf{x}, \boldsymbol{\theta}) = \mu_s(\mathbf{x}) \left(u(\mathbf{x}, \boldsymbol{\theta}) - \int_{S^{n-1}} k(\boldsymbol{\theta} \cdot \boldsymbol{\theta}') u(\mathbf{x}, \boldsymbol{\theta}') d\boldsymbol{\theta}' \right). \quad (2)$$

Here, $\mu_s(\mathbf{x}) \in L^\infty(\mathcal{D})$ is the scattering coefficient and $d\boldsymbol{\theta}$ is the surface measure on S^{n-1} normalized so that $\int_{S^{n-1}} d\boldsymbol{\theta} = 1$. The scattering kernel $k(\boldsymbol{\theta} \cdot \boldsymbol{\theta}')$, which describes the probability that photons traveling in direction $\boldsymbol{\theta}'$ scatter into direction $\boldsymbol{\theta}$, is a positive function independent of \mathbf{x} and satisfies the normalization condition:

$$\int_{S^{n-1}} k(\boldsymbol{\theta} \cdot \boldsymbol{\theta}') d\boldsymbol{\theta}' = 1. \quad (3)$$

The scattering kernel for light propagation in tissues is chosen here as the Henyey-Greenstein phase function²²

$$k(\boldsymbol{\theta} \cdot \boldsymbol{\theta}') = \frac{1 - g^2}{(1 + g^2 - 2g \cos \phi)^{3/2}}, \quad (4)$$

where ϕ is the angle between $\boldsymbol{\theta}$ and $\boldsymbol{\theta}'$, i.e., $\boldsymbol{\theta} \cdot \boldsymbol{\theta}' = \cos \phi$ and where $g \in [-1, 1]$ is the anisotropy factor, which measures how forward peaked the phase function is. The larger g is, the more forward the scattering. The anisotropy factor is often used to define the so-called effective scattering coefficient through $\mu'_s = (1 - g)\mu_s$.

The method for discretizing the ERT in this paper is based on the combination of the discrete ordinates method²³ for angular variable and a finite volume method for space variable.²⁴ In the discrete ordinates method,²³ we approximate the total scalar flux, defined as the integral of $u(\mathbf{x}, \boldsymbol{\theta})$ over S^{n-1} , by the following quadrature rule

$$\int_{S^{n-1}} u(\mathbf{x}, \boldsymbol{\theta}) d\boldsymbol{\theta} \approx \sum_{j=1}^J \eta_j u(\mathbf{x}, \boldsymbol{\theta}_j), \quad (5)$$

where $\boldsymbol{\theta}_j$ is the j th direction and η_j the associated weight, for $1 \leq j \leq J$. To ensure particle conservation, we ensure that

$$\sum_{j=1}^J \eta_j = 1. \quad (6)$$

The equation of radiative transfer is now decomposed as a discrete set of J coupled differential equations that describe the photon flux field along J directions:

$$\nabla \cdot (\boldsymbol{\theta}_j u) + (\mu_t + \frac{i\omega}{v})u(\mathbf{x}, \boldsymbol{\theta}_j) = \mu_s(\mathbf{x}) \sum_{j'=1}^J \eta_{j'} k_{jj'} u(\mathbf{x}, \boldsymbol{\theta}_{j'}), \quad (7)$$

for $j = 1, 2, \dots, J$, where $k_{jj'} = k(\boldsymbol{\theta}_j \cdot \boldsymbol{\theta}_{j'})$, and where $\mu_t = \mu_a + \mu_s$. We impose

$$\sum_{j=1}^J \eta_j k_{jj'} = 1, \quad 1 \leq j' \leq J, \quad (8)$$

so that the number of photons in the system is preserved by the scattering process.

We now integrate the above discrete ordinates equations (7) over a cell \mathcal{C} of a finite volume mesh, and use the divergence theorem on the first term. We obtain the following equations

$$\int_{\partial\mathcal{C}} \boldsymbol{\theta}_j \cdot \mathbf{n}_{\mathcal{C}}(\mathbf{x}) u_j d\gamma(\mathbf{x}) + (\mu_t^{\mathcal{C}} + \frac{i\omega}{v}) V_{\mathcal{C}} u_j^{\mathcal{C}} = V_{\mathcal{C}} \mu_s^{\mathcal{C}} \sum_{j'=1}^J \eta_{j'} k_{jj'} u_{j'}^{\mathcal{C}}, \quad (9)$$

for $j = 1, 2, \dots, J$, where, $\mathbf{n}_{\mathcal{C}}(\mathbf{x})$ denotes the outward normal to $\partial\mathcal{C}$ at point $\mathbf{x} \in \partial\mathcal{C}$, $d\gamma(\mathbf{x})$ denotes the surface Lebesgue measure on $\partial\mathcal{C}$ and $\mu_s^{\mathcal{C}}$ ($\mu_t^{\mathcal{C}}$) is the value of μ_s (μ_t) on cell \mathcal{C} .

After introduce a first order approximation of the flux term $\int_{\partial\mathcal{C}} \boldsymbol{\theta}_j \cdot \mathbf{n}_{\mathcal{C}}(\mathbf{x}) u_j d\gamma(\mathbf{x})$, and collecting the results over all control volumes, we arrive at the following system of complex-valued algebraic equations

$$\mathbf{A}\mathbf{U} = \mathbf{S}\mathbf{U} + \mathbf{F} \quad (10)$$

where $\mathbf{A} \in \mathbb{C}^{NJ \times NJ}$ and $\mathbf{S} \in \mathbb{C}^{NJ \times NJ}$ are the discretized streaming-collision and scattering operators, respectively. The vector $\mathbf{U} \in \mathbb{C}^{NJ \times 1}$ contains the values of $u(\mathbf{x}, \boldsymbol{\theta})$ on the different cells and directions.

We solve the algebraic equations (10) by a restarted generalized minimal residual (GMRES) algorithm.²⁵ More details on the numerical methods mentioned here can be found elsewhere.^{26, 27}

2.2. Reconstructoin algorithms

Let us denote from now on by $\mu_a \in \mathbb{R}^{N \times 1}$ the absorption coefficient vector $(\mu_a^1, \dots, \mu_a^C, \dots, \mu_a^N)^T$ and $\mu_s \in \mathbb{R}^{N \times 1}$ the scattering coefficient vector $(\mu_s^1, \dots, \mu_s^C, \dots, \mu_s^N)^T$.

We solve the inverse problem of optical tomography by minimizing the following objective function

$$\mathcal{F}_{\alpha}(\mu_a, \mu_s) = \frac{1}{2} \sum_{s=1}^{N_s} \sum_{d=1}^{N_d} |\mathcal{P}_d \mathbf{U}_s - z_d^{\delta}|^2 + \frac{\alpha}{2} \sum_{\mathcal{C}=1}^N \sum_{p=\{a,s\}} \left(\sum_{\kappa=\{x,y,z\}} (\mathcal{D}_{\kappa}^{\mathcal{C}} \mu_p)^2 + (\mu_p^{\mathcal{C}})^2 \right), \quad (11)$$

where N_s and N_d are the total number of sources and detectors. z_d^{δ} is the measurement with noise level δ . Here $\mathcal{D}_{\kappa}^{\mathcal{C}} \in \mathbb{R}^{1 \times N}$ denotes the discretized partial differential operator at cell \mathcal{C} in the κ ($= x, y, z$) direction. $\mathcal{P}_d \in \mathbb{R}^{1 \times N}$ is a discretized version of the measurement operator. The last term is a regularization term which is essentially the summation of the \mathcal{H}_1 norm of μ_a and μ_s , and α is the regularization parameter.²⁸

We have implemented a special kind of quasi-Newton method, the limited-memory version of the Broyden-Fletcher-Goldfarb-Shanno (BFGS) algorithm²⁹⁻³¹ to minimize the above functional. The gradient of the objective function to μ_a and μ_s in each cell, which is used by the BFGS algorithm, is calculated by the following formula

$$\frac{\partial \mathcal{F}_\alpha}{\partial \mu_a^c} = \sum_{s=1}^{N_s} \left[\mathbf{V}_s^T \frac{\partial(\mathbf{A} - \mathbf{S})}{\partial \mu_a^c} \mathbf{U}_s \right]_{\text{Re}} + \alpha \left(\sum_{\kappa=\{x,y,z\}} (\mathcal{D}_\kappa^c \mu_a) (\mathcal{D}_\kappa^c \mathcal{I}_C) + \mu_a^c \right). \quad (12)$$

$$\frac{\partial \mathcal{F}_\alpha}{\partial \mu_s^c} = \sum_{s=1}^{N_s} \left[\mathbf{V}_s^T \frac{\partial(\mathbf{A} - \mathbf{S})}{\partial \mu_s^c} \mathbf{U}_s \right]_{\text{Re}} + \alpha \left(\sum_{\kappa=\{x,y,z\}} (\mathcal{D}_\kappa^c \mu_s) (\mathcal{D}_\kappa^c \mathcal{I}_C) + \mu_s^c \right). \quad (13)$$

where \mathbf{V}_s solves the adjoint problem

$$(\mathbf{A} - \mathbf{S})^T \mathbf{V}_s = - \sum_{d=1}^{N_d} \overline{(\mathcal{P}_d \mathbf{U}_s - z_d^\delta)} \mathcal{P}_d^T. \quad (14)$$

The unit direction vector $\mathcal{I}_C \in \mathbb{R}^{N \times 1}$ is a vector whose C -th element is 1 and all other components are zero. We refer interested readers to [29-31] for more details on the BFGS algorithms, and to [27] for more details on some theoretical and numerical aspects of the reconstruction problem.

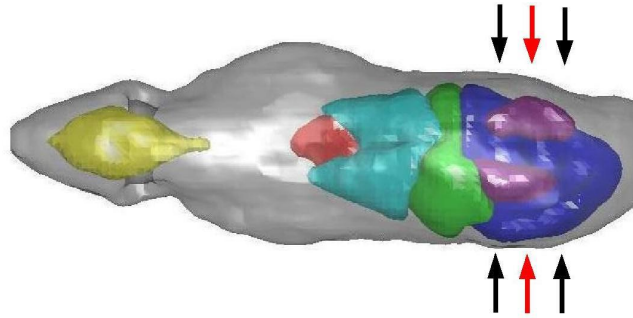


Figure 1. Coronal view of the virtual mouse model with organs.

Tissue	μ_a (cm^{-1})	μ'_s (cm^{-1})
Brain	0.30	15.0
GI track	0.27	12.5
Heart	0.10	5.00
Kidney	0.67	6.00
Liver	0.33	5.00
Lung	0.81	20.0
Skin	0.67	22.5

Table 1. Optical properties for the organs of the numerical mouse model.

2.3. The numerical mouse model

To test the utility of the aforementioned optical imaging algorithm for small animal imaging, we have furthermore developed a numerical phantom of a mouse. The mouse model was created from 90 axial magnetic resonance images with a slice separation of 0.6mm. Each image was segmented into a whole mouse section by thresholding in combination with some minimal manual smoothing. Subsequently, some large internal organs and structures were segmented by hand. The set of images were then aligned so that the 3D image axes corresponded to an intuitive physiological coordinate system. Interpolation was performed in the axial x-y plane to reduce the resolution to 0.6 mm, which matches the slice separation in the z-direction. In this way the model consists of voxels with equal physical side length. Edge information was extracted using custom software. Finally, a cubic mesh was defined from the 3D image data using custom software. The final mouse mesh consists of 36217 nodes that form 31457 cubic control volumes (see Figure 1). Different optical properties can be assigned to different individual organs. The values for μ_a and μ_s used in this study can be found in Table 1.

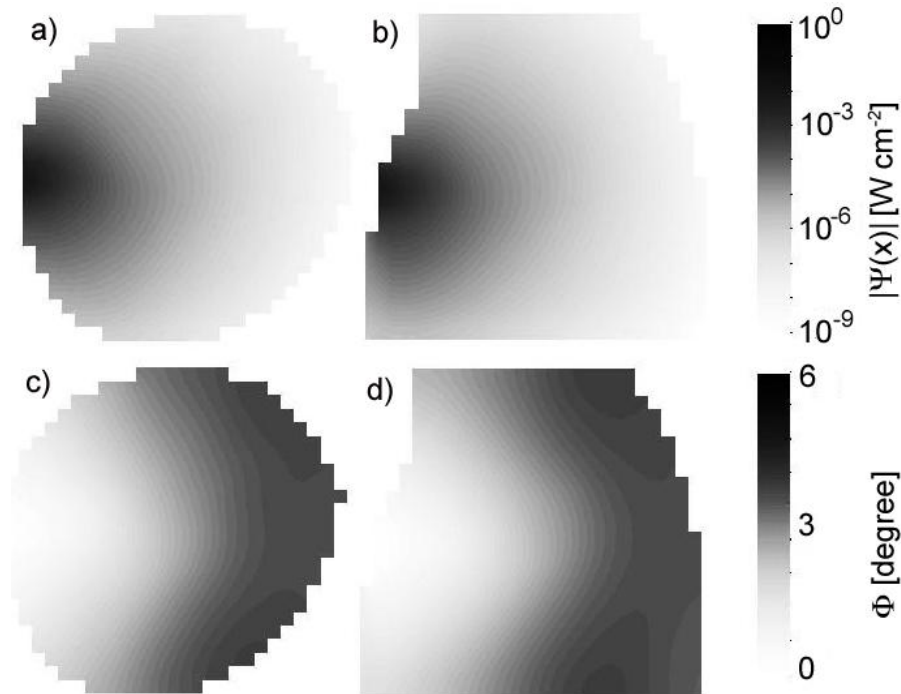


Figure 2. Axial (a & c) and coronal (b & d) of the fluence (a & b) and phase-shift (c & d) distributions at $\omega = 100\text{MHz}$.

3. RESULTS

3.1. Forward simulations

We first investigated the influence of different source modulation frequencies on the fluence and phase-delay distributions in the mouse model. Before doing that, let's first specify what we means by fluence and phase-delay. We introduce the complex function $\Psi(\mathbf{x})$ defined as

$$\Psi(\mathbf{x}) = \int_{S^{n-1}} u(\mathbf{x}, \boldsymbol{\theta}) d\boldsymbol{\theta}. \quad (15)$$

The fluence $|\Psi(\mathbf{x})|$ and the phase $\Phi(\mathbf{x})$ are then defined through $\Psi(\mathbf{x}) = |\Psi(\mathbf{x})|e^{i\Phi(\mathbf{x})}$. Figure 2 and Figure 3 show these distributions calculated at $\omega = 100\text{MHz}$ and $\omega = 600\text{MHz}$, respectively. We observe that the major difference between the two cases is the phase delay distribution. In the case of $\omega = 100\text{MHz}$, the maximal phase delay is only ~ 5 degree, while in the case of $\omega = 600\text{MHz}$ a maximal phase shift of ~ 25 degree occurs. From the

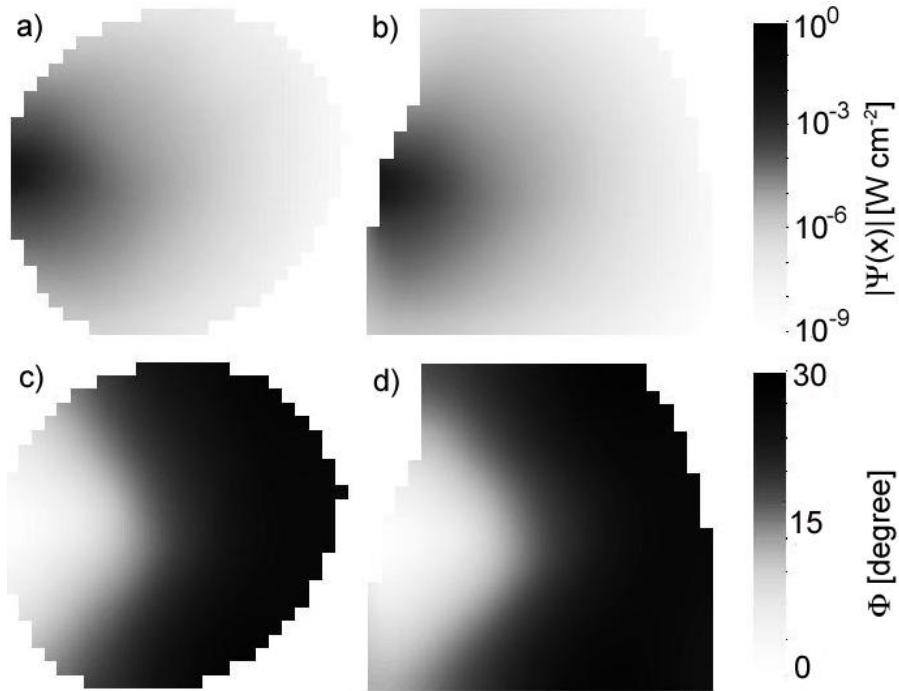


Figure 3. Axial (a & c) and coronal (b & d) of the fluence (a & b) and phase-shift (c & d) distributions at $\omega = 600\text{MHz}$.

experimental point of view, if we can perform measurement up to the accuracy of one degree,³²⁻³⁶ then in the case of $\omega = 100\text{MHz}$, the error in our measurement is at least 20% (5 degree is maximum phase delay!), while in the case of $\omega = 600\text{MHz}$, this error reduces to $\sim 4\%$.

To further explore the effect of different modulation frequency, we compute the sensitivity of our measurements (both fluence and phase delay) to a change of optical properties in the kidney. By doubling μ_a for the kidneys

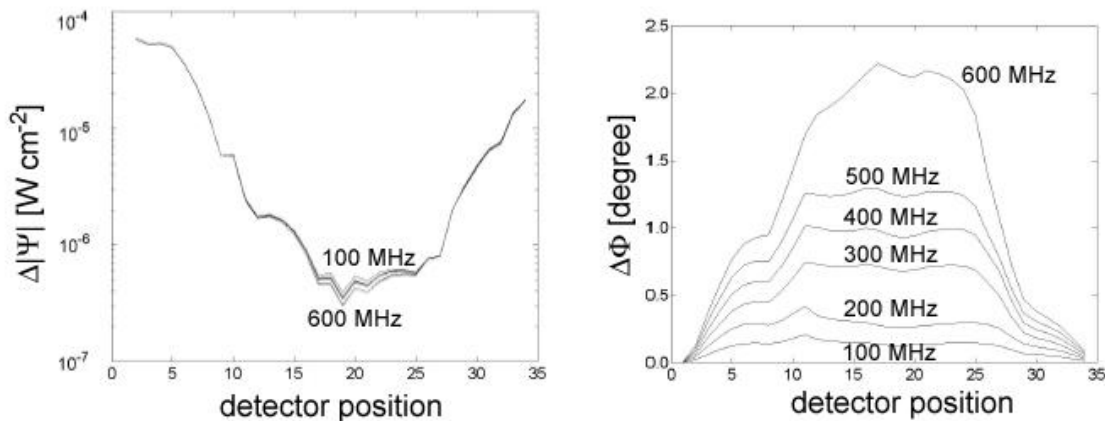


Figure 4. Differences in fluence (left) and phase delay (right) caused by a doubling of the absorption coefficient of the kidneys. Values are given for modulation frequencies between 100 and 600 MHz for all detector positions on the surface of the mouse model.

we mimics the situation of a growing kidney tumor, in which neovascularizations leads to an increased blood volume in the affected kidney (for more details see³⁷). The results are presented in Figure 4. Here we show the differences of fluence and phase between calculations with optical properties list in Table 1 (“healthy mouse”) and the calculation with doubled μ_a for the kidneys (mouse with kidney tumor). The result shows that we need frequencies well above 100MHz to be able to see measurable phase shifts that let us distinguish between a “healthy” mouse and a mouse with “tumors”.

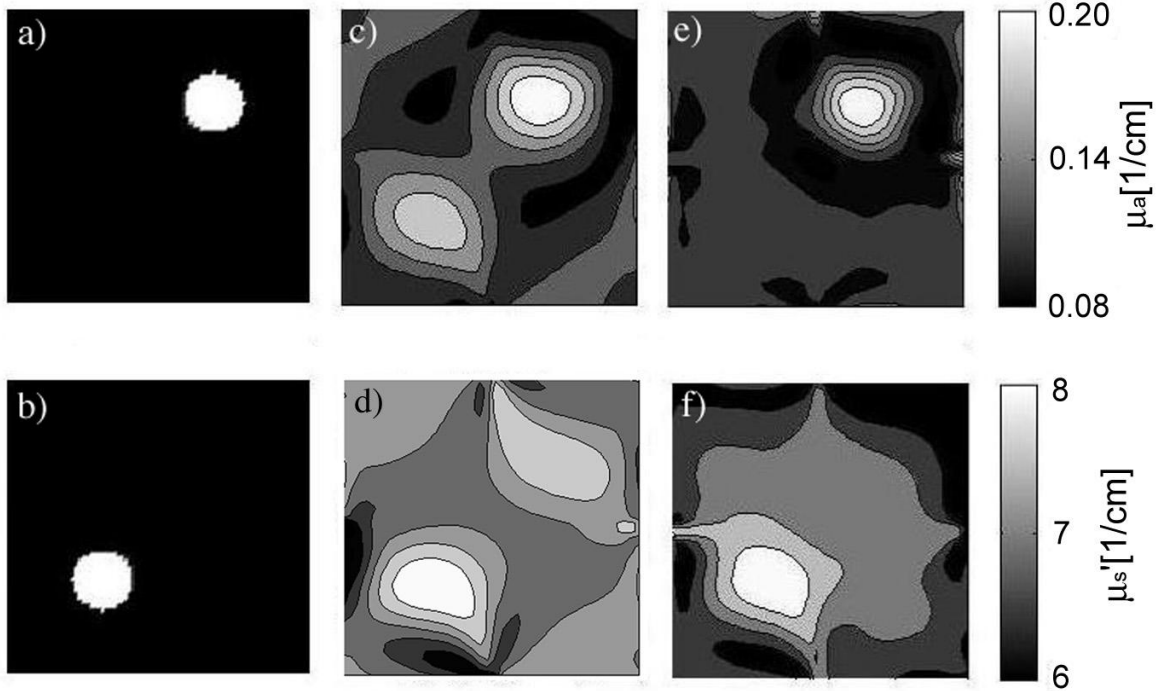


Figure 5. Frequency domain versus steady-state domain image reconstruction. a) original map of spatial distribution of the absorption coefficient μ_a ; b) original map of spatial distribution of the scattering coefficient μ'_s ; c) & d) reconstruction results using steady-state data ($\omega = 0$ MHz); e) & f) reconstruction results using FD data at a source modulation frequency of $\omega = 600$ MHz. For the reconstructions data from 4 source and 16 detectors equally distributed on the circumference of the $2 \times 2\text{cm}^2$ square was used. All reconstruction started with an initial guess of a homogeneous medium with $\mu_a = 0.12\text{ cm}^{-1}$ and $\mu'_s = 7.2\text{ cm}^{-1}$. Clearly visible is the cross-talk between absorption and scattering effects in the images c) & d) that were obtain from steady state data ($\omega = 0$ MHz).

3.2. Preliminary reconstructions

To illustrate how higher source modulation frequencies lead to a better separation between absorption and scattering effects, we first performed simulations on a simple model, shown in Figure 5 a,b. The medium consists of a 2×2 square that contains one circular absorption as well as one circular scattering inhomogeneity in different locations. Generating noise-free synthetic data at $\omega = 0\text{MHz}$ as well $\omega = 600\text{MHz}$ for this medium, we employed our transport-theory-based image reconstruction algorithm to reconstruct the optical property distributions. Starting both reconstructions with the same initial guess, we clearly see that a better separation of scattering and absorption effects is obtained when a higher source modulation frequency is used (see Figure 5 e & f).

In a second example, we performed reconstructions using the numerical mouse model. In this case we doubled the absorption coefficient of the kidney while keeping all the other parameters the same as those in Table 1. Synthetic data was generated using 3 layers of source and detectors. All 4 sources were located in the middle layer, while the 72 detectors were distributed equally on the three layers. The location of the three layers of source and detectors are illustrated by those arrows in Figure 1.

Absorption-coefficient reconstruction results are presented in Figure 6 and Figure 7 for the case of $\omega = 100\text{MHz}$ and $\omega = 600\text{MHz}$, respectively. One can see that at the higher modulation frequency the kidneys are better resolved and the values of the absorption coefficients are recovered more accurately.

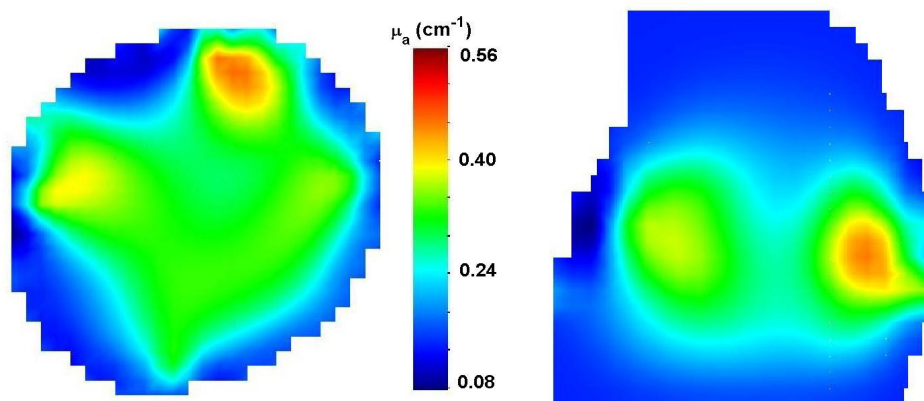


Figure 6. Axial (left) and coronal (right) cuts of reconstructed highly absorbing kidneys of the virtual mouse model ($\omega=100\text{MHz}$).

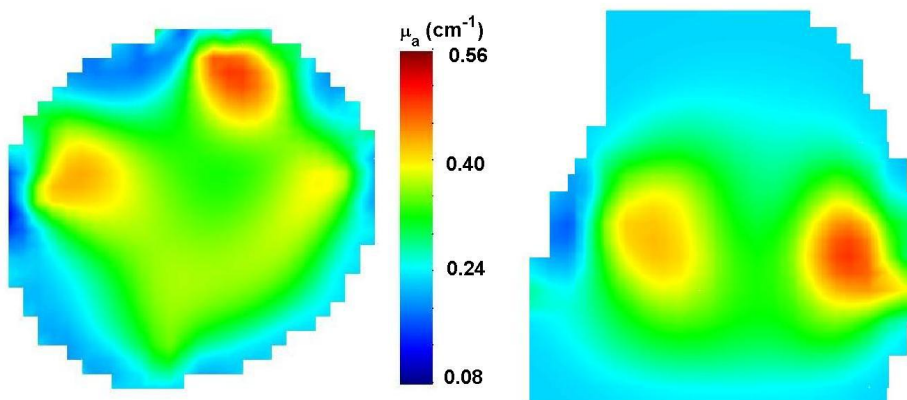


Figure 7. Axial (left) and coronal (right) cuts of reconstructed highly absorbing kidneys of the virtual mouse model ($\omega=600\text{MHz}$).

4. SUMMARY

We have developed a model-based iterative image reconstruction scheme based on the equation of radiative transfer in the frequency domain for the applications in small animal optical tomography. To test the utility of such a code in small animal imaging we have furthermore developed a numerical phantom of a small animal. We found by several numerical simulations that to make truly use of phase information in the reconstruction process modulation frequencies well above 100 MHz are necessary. Only at these higher frequencies the phase shifts introduced by the lesions of interest are large enough to be measured. For smaller frequencies no substantial improvements over steady-state systems can be expected

ACKNOWLEDGMENTS

This work is supported in part by the National Institute of Biomedical Imaging and Bioengineering (grant R01 EB001900-01), which is a division of the National Institute of Health. We also would like to thank Dr. Abdoulaev, Columbia University, for his helpful comments and advise in developing the transport-theory based algorithms.

REFERENCES

1. P. D. Acton and H. Kung, "Small animal imaging with high resolution single photon emission tomography," *Nuclear Medicine and Biology* **30**, pp. 889–895, 2003.
2. S. R. Cherry, "In vivo molecular imaging and genomic imaging: new challenges for imaging physics," *Phys. Med. Biol.* **49**, pp. R13–R48, 2004.
3. I. K. Chun, M. H. Cho, S. C. Lee, M. H. Cho, and S. Y. Lee, "X-ray micro-tomography system for small-animal imaging with zoom-in imaging capability," *Phys. Med. Biol.* **49**, pp. 3889–3902, 2004.
4. J. Dazai, N. A. Bock, B. J. Nieman, L. M. Davidson, R. M. Henkelman, and X. J. Chen, "Multiple mouse biological loading and monitoring system for mri," *Magnetic resonance in medicine* **52**, pp. 709–715, 2004.
5. M. G. Pomper, "Can small animal imaging accelerate drug development?," *J. Cellular Biochemistry Suppl.* **39**, pp. 211–220, 2002.
6. T. Zeniya, H. Watabe, T. Aoi, K. M. Kim, N. Teramoto, T. Hayashi, A. Sohlberg, H. Kudo, and H. Iida, "A new reconstruction strategy for image improvement in pinhole spect," *European Journal of Nuclear Medicine and Molecular Imaging* **31**, pp. 1166–1172, 2004.
7. A. H. Hielscher, "Optical tomographic imaging of small animals," *Current Opinion in Biotechnology* **16**, pp. 79–88, 2005.
8. A. Y. Bluestone, M. Stewart, B. Lei, I. S. Kass, J. Lasker, G. Abdoulaev, and A. H. Hielscher, "Three-dimensional optical tomographic brain imaging in small animals, part I: Hypercapnia," *Journal of Biomedical Optics* **9**, pp. 1046–1062, 2004.
9. A. Y. Bluestone, M. Stewart, J. Lasker, G. Abdoulaev, and A. H. Hielscher, "Three-dimensional optical tomographic brain imaging in small animals, part ii: Unilateral carotid occlusion," *Journal of Biomedical Optics* **9**, pp. 1063–1073, 2004.
10. J. P. Culver, T. Durduran, D. Furuya, C. Cheung, J. H. Greenberg, and A. G. Yodh, "Diffuse optical tomography of cerebral blood flow, oxygenation, and metabolism in rat during focal ischemia," *Journal of Cerebral Blood Flow & Metabolism* **23**, pp. 911–924, 2003.
11. G. Yu, T. Durduran, D. Furuya, J. H. Greenberg, and A. G. Yodh, "Frequency-domain multiplexing system for in vivo diffuse light measurements of rapid cerebral hemodynamics," *Applied Optics* **42**, pp. 2931–2939, 2003.
12. E. E. Graves, R. Weissleder, and V. Ntziachristos, "Fluorescence molecular imaging of small animal tumor models," *Current Molecular Medicine* **4**, pp. 419–430, 2004.
13. V. Ntziachristos, E. A. Schellenberger, J. Ripoll, D. Yessayan, E. Graves, A. Bodganov, L. Josephson, and R. Weissleder, "Visualization of antitumor treatment by means of fluorescence molecular tomography with an annexin v-cy5.5 conjugate," *PNAS* **33**, pp. 12294–12299, 2004.
14. T. O. McBride, B. W. Pogue, U. L. Österberg, and K. D. Paulsen, "Separation of absorption and scattering heterogeneities in NIR tomographic imaging of tissue," in *OSA Technical Digest, Optical Society of America*, (Washington DC), 2000. Biomedical Topical Meetings.
15. A. D. Kim and A. Ishimaru, "Optical diffusion of continuous-wave, pulsed and density waves in scattering media and comparisons with radiative transfer," *Applied Optics* **37**, pp. 5313–5319, 1998.
16. R. Elaloufi, R. Carminati, and J. Greffet, "Time-dependent transport through scattering media: from radiative transfer to diffusion," *J. Opt. A: Pure Appl. Opt.* **4**, pp. S103–S108, 2002.
17. A. H. Hielscher, R. E. Alcouffe, and R. L. Barbour, "Comparison of finite-difference transport and diffusion calculations for photon migration in homogeneous and heterogeneous tissue," *Phys. Med. Biol.* **43**, pp. 1285–1302, 1998.
18. H. Dehghani, D. T. Delpy, and S. R. Arridge, "Photon migration in non-scattering tissue and the effects on image reconstruction," *Phys. Med. Biol.* **44**(12), pp. 2879–2906, 1999.

19. M. Firbank, S. R. Arridge, M. Schweiger, and D. T. Delpy, "An investigation of light transport through scattering bodies with non-scattering regions," *Phys. Med. Biol.* **41**, pp. 767–783, 1996.
20. E. Okada, M. Firbank, M. Schweiger, S. R. Arridge, M. Cope, and D. T. Delpy, "Theoretical and experimental investigation of near-infrared light propagation in a model of the adult head," *Appl. Opt.* **36**(1), pp. 21–32, 1997.
21. S. R. Arridge, "Optical tomography in medical imaging," *Inverse Problems* **15**, pp. R41–R93, 1999.
22. L. G. Henyey and J. L. Greenstein, "Diffuse radiation in the galaxy," *Astrophys. J.* **90**, pp. 70–83, 1941.
23. E. E. Lewis and W. F. Miller, *Computational Methods of Neutron Transport*, American Nuclear Society, La Grange Park, IL, 1993.
24. R. Eymard, T. Gallouet, and R. Herbin, "Finite volume methods," in *Handbook of Numerical Analysis VII*, P. Ciarlet and J. L. Lions, eds., North-Holland, Amsterdam, 2000.
25. Y. Saad and M. H. Schultz, "GMRES: A generalized minimal residual algorithm for solving nonsymmetric linear systems," *SIAM J. Sci. Stat. Comput.* **7**, pp. 856–869, 1986.
26. K. Ren, G. Abdoulaev, G. Bal, and A. H. Hielscher, "Algorithm for solving the equation of radiative transfer in the frequency domain," *Optics Lett.* **29**, pp. 578–580, 2004.
27. K. Ren, G. Bal, and A. H. Hielscher, "Frequency domain optical tomography based on the equation of radiative transfer." submitted to *SIAM J. Sci. Comput.*, 2004.
28. H. W. Engl, M. Hanke, and A. Neubauer, *Regularization of Inverse Problems*, Kluwer Academic Publishers, Dordrecht, 1996.
29. A. D. Klose and A. H. Hielscher, "Quasi-newton methods in optical tomographic image reconstruction," *Inverse Problems* **19**, pp. 387–409, 2003.
30. C. T. Kelley, *Iterative Methods for Optimization*, Frontiers in Applied Mathematics, Society of Industrial and Applied Mathematics, Philadelphia, 1999.
31. J. Nocedal and S. J. Wright, *Numerical Optimization*, Springer-Verlag, New York, 1999.
32. B. Chance, M. Cope, E. Gratton, N. Ramanujam, and B. Tromberg, "Phase measurement of light and absorption and scattering in human tissue," *Rev. Scientific Instruments* **69**, pp. 3457–3481, 1998.
33. A. Godavarty, M. Eppstein, C. Y. Zhang, S. Theru, A. B. Thompson, M. Gurfinkel, and E. M. Sevick-Muraca, "Fluorescence-enhanced optical imaging in large tissue volumes using a gain-modulated iccd camera," *Physics in Medicine and Biology* **48**, pp. 1701–1720, 2003.
34. I. Nissilä, K. Kotilahti, K. Fallström, and T. Katila, "Instrumentation for the accurate measurement of phase and amplitude in optical tomography," *Rev. Sci. Instrum.* **73**(9), pp. 3306–3312, 2002.
35. N. Ramanujam, C. Du, H. Y. Ma, and B. Chance, "Sources of phase noise in homodyne and heterodyne phase modulation devices used for tissue oximetry studies," *Rev. Scientific Instruments* **69**, pp. 3042–3054, 1998.
36. A. B. Thompson and E. Sevick-Muraca, "Near-infrared fluorescence contrast-enhanced imaging with intensified charge-coupled device homodyne detection: measurement precision and accuracy," *J. Biomedical Optics* **8**, pp. 111–120, 2003.
37. J. Masciotti, G. Abdoulaev, J. Hur, J. Papa, J. Bae, J. Kandel, and A. Hielscher, "Combined optical tomographic and magnetic resonance imaging of small animals," *This SPIE proceedings (in press)* .